

Fe-N-doped mesoporous carbon loaded on reduced graphene oxides with dual active sites for efficient oxygen reduction catalysts

*Chao Zhang^{a, b}, Jun Liu^a, Yixing Ye^a, Zabeada Aslam^c, Rik Drummond-Brydson^c and
Changhao Liang^{a, b*}*

^a Key Laboratory of Materials Physics and Anhui Key Laboratory of Nanomaterials and Nanotechnology, Institute of Solid State Physics, Hefei Institutes of Physical Science, Chinese Academy of Sciences, Hefei, 230031, China

^b University of Science and Technology of China, Hefei, 230026, China

^c Institute for Materials Research, School of Chemical and Process Engineering, University of Leeds, Leeds LS2 9JT, UK

E-mail: chliang@issp.ac.cn

ABSTRACT:

Transition metal/nitrogen/carbon (M-N/C) catalysts are considered as one of the most promising candidates to replace Pt/C catalysts for oxygen reduction reactions (ORR). Here, we have designed novel reduced graphene oxides (rGO) supported Fe-N-doped carbon (Fe-N-C/rGO) catalysts via simple pyrolysis of polypyrrole(Ppy)-FeO-GO composites. The as-prepared catalysts induced an onset potential of 0.94 V, a half-wave potential of 0.81 V in alkaline solutions, which is much better than that of the counterpart N-C and N-C/rGO catalysts, and comparable to that of Pt/C catalysts. Moreover, the Fe-N-C/rGO catalysts showed improved durability and higher tolerance against methanol crossover than Pt/C in alkaline solutions. This superior ORR performance can be ascribed to the combined catalytic effect of both Fe-based nanoparticles (Fe_3O_4 , Fe_4C) and Fe-N_x sites, as well as fast mass transfer and accessible active sites benefitting from the mesoporous structure and high specific surface area. This work provides new insight for synthesis of a more promising non-platinum electrocatalyst for metal-air batteries and fuel-cell applications.

KEYWORDS: porous carbon; Fe-N-C catalyst; dual active sites; oxygen reduction reaction; electrocatalysis

INTRODUCTION

The depletion of fossil fuels and deterioration of the natural environment have triggered significant research on sustainable energy storage and conversion systems, such as metal-air batteries and fuel cells.¹⁻³ However, the slow kinetics of the oxygen reduction reaction (ORR) at the cathode has limited the widespread commercialization of these renewable energy systems.^{4,5} To date, Pt-based materials are considered as the most efficient electrocatalysts for ORR. Unfortunately, the limited reserve and prohibitive cost of Pt-based materials limit their large-scale application. Moreover, their low durability and poor tolerance to methanol result in the loss of performance. Accordingly, increased efforts are focused on developing nonprecious metal catalysts with low-cost and comparable performance to Pt.^{6,7}

To design effective nonprecious metal catalysts with comparable performance to that of the state-of-the-art Pt/C catalyst, two crucial factors need to be considered. First, the intrinsic nature of active sites, which are determined by the catalyst composition. Second, the specific surface area and porous structure, which determine the mass transfer during the reaction process and hence the accessible part of the active sites.⁸⁻¹⁰ In order to obtain such highly efficient ORR electrocatalysts, various non-precious metal catalysts have been developed, including transition-metal-coordinating macrocyclic compounds,¹¹ pyrolyzed metal/nitrogen/carbon (M-N/C) catalysts,^{12,13} metal oxides and chalcogenides,¹⁴⁻¹⁶ and heteroatom-doped carbon materials.^{17,18} Amongst these, the M-N/C (M=Fe, Co, etc.) catalyst system, containing metal-nitrogen coordinating active sites on the surface, are considered one of the most promising catalysts to replace Pt.^{19,20}

Generally, direct pyrolysis of the precursors which contain carbon, nitrogen and transition

metal, like MOFs,²¹⁻²³ is the most common method used to prepare M-N/C catalysts. However, severe aggregation of products prepared by this method occurs during the pyrolysis process, which results in a sharp decrease of the specific surface area and destruction of the porous structure, thereby impeding mass transfer during the reaction process, and leading to a decline of the ORR activity. To overcome this aggregation, loading the M-N/C catalysts onto graphene or graphene-like two-dimensional nanosheet materials has been employed, which not only increases the specific surface area for a higher catalytic activity, but also retains the porous structure promoting mass transfer.²⁴⁻²⁷ Therefore, exploring new synthesis strategies for rGO supported M-N/C catalysts is of interest to optimise ORR performance.

Here, we have prepared Fe-N-C/rGO composites with a sheet-like structure by simple pyrolysis of polypyrrole(Ppy)-FeO-GO composites. The as-prepared Fe-N-C/rGO catalysts possessed a mesoporous structure, high specific surface area and many active sites resulting in excellent ORR performance, which is comparable to that of Pt/C catalysts in alkaline media. More importantly, Fe-N-C/rGO show better durability and higher tolerance against methanol crossover than Pt/C in alkaline media, suggesting that it could represent an alternative catalyst material.

EXPERIMENTAL SECTION

Chemical reagents and materials

All chemicals were of analytical grade and used without further purification. Acetone and ammonium persulfate were purchased from Sinopharm Chemical Reagent Co. Ltd (China). The pyrrole monomer was purchased from Aladdin Industrial Corporation (Shanghai, China). Twenty percent Pt/C catalysts were purchased from Alfa Aesar. Deionized water

(resistance, $>18 \text{ M}\Omega \text{ cm}^{-1}$) was used for all experiments work.

Synthesis of Fe-N-C/rGO electrocatalysts

GO was first synthesized according to a modified Hummers method.^{28,29} The colloidal solution consisted of FeO NPs prepared by a laser ablation in liquid (LAL) method. Scheme 1 shows that an iron plate was fixed in a vessel filled with 16 mL acetone. The rotating metal plate was ablated for 60 min by a focused laser (1064 nm) with a 10 Hz pulse repetition rate and 100 mJ pulse energy. After laser ablation, the fresh colloid was mixed with GO and the precipitate was collected by centrifugation and dispersed in 20 mL deionized water to form a uniform colloidal solution. Then 10 μL pyrrole monomer was added into the colloidal solution and stirred for 30 min. Subsequently, 114.1 mg $(\text{NH}_4)_2\text{S}_2\text{O}_8$ was added to the above solution with continuous stirring for 12 h. The product was collected by centrifugation and dried at 50 $^\circ\text{C}$ in a vacuum chamber. The final product was heated to 800 $^\circ\text{C}$ for 2 h under flowing N_2 atmosphere with a heating rate of 5 $^\circ\text{C min}^{-1}$. As reference catalyst, N-C/rGO was also synthesized without the addition of the FeO colloid.

Materials characterization

Transmission electron microscopy (TEM) investigations were conducted using a FEI Tecnai TF20 operated at 200 kV. High-angle annular dark-field (HAADF) scanning TEM (STEM) imaging and STEM/EDX-mapping was undertaken on a FEI Titan-Themis³ at 300 kV. Scanning electron microscopy (SEM) measurements were conducted using a field-emission Hitachi SU8020. X-ray diffraction (XRD) was performed on a Philips X'Pert system with Cu $K\alpha$ radiation ($\lambda=1.5419 \text{ \AA}$). X-ray photoelectron spectroscopy (XPS) using a Thermo ESCALAB 250 was used to analyse the surface chemical state. The specific surface

area, pore volume and pore size distribution were estimated by nitrogen adsorption at 77 K (Tristar 3020M), using the Brunauer-Emmett-Teller (BET) and the Barrett-Joyner-Halenda (BJH) methods. Raman spectra were collected using a Renishaw in-Via instrument with an Ar laser source of 532 nm in a macroscopic configuration.

Electrochemical Measurements

All the electrochemical measurements were conducted on a Zahner electrochemical workstation (IM6) equipped with a rotating disk electrode (RDE) system (ALS, Japan) as part of a three-electrode system; a Pt wire and a KCl-saturated Ag/AgCl electrode were used as the counter and reference electrodes, respectively, with the 3 mm diameter RDE coated with the catalyst film serving as the working electrode. Initially the rotating disk electrode was polished with Al₂O₃ slurry and ultrasonically cleaned in ethanol for a few minutes. The Fe-N-C/rGO catalyst ink was prepared by ultrasonically dispersing 1.5 mg of the catalyst powder in 300 μ L deionized water. Then 5 μ L of the catalyst ink was deposited onto the polished RDE. After drying the electrode in an ambient environment for 24 h, 20 μ L of Nafion solution was dropped onto the dried sample.

The ORR performance of the Fe-N-C/rGO was evaluated in an Ar- and O₂-saturated 0.1 M KOH aqueous solution. All the potentials were calibrated to the potentials versus the reversible hydrogen electrode (RHE) according to following equation:

$$E(\text{vs. RHE}) = E(\text{vs. Ag/AgCl}) + 0.197 + 0.059\text{pH} \quad (1)$$

The electron transfer number during the ORR was determined by the Koutechy-Levich equation:

$$\frac{1}{J} = \frac{1}{J_L} + \frac{1}{J_K} = \frac{1}{B\omega^{1/2}} + \frac{1}{J_K} \quad (2)$$

$$B = 0.62nFC_0(D_0)^{2/3}\nu^{-1/6} \quad (3)$$

where J is the measured current density, J_K is the kinetic current density, J_L is the diffusion-limited current density, ω is the electrode rotation rate and, F is the Faraday constant (96485 C mol^{-1}). C_0 is the bulk concentration of O_2 ($1.2 \times 10^{-3} \text{ mol L}^{-1}$ for 0.1 M KOH solution), D_0 is the diffusion coefficient of O_2 ($1.9 \times 10^{-5} \text{ cm}^2 \text{ s}^{-1}$ for 0.1 M KOH solution), and ν is the kinetic viscosity of the electrolyte ($0.01 \text{ cm}^2 \text{ s}^{-1}$ for 0.1 M KOH aqueous solution).

RESULTS AND DISCUSSION

As shown in Scheme 1, laser ablation of an Fe target in acetone was used to produce a yellow Fe-based colloidal solution (inset in Figure S1a). The corresponding XRD pattern (Figure S1a) exhibits diffraction peaks which index well to FeO (JCPDF No. 01-1223). Subsequently, the FeO colloidal dispersion was mixed with a GO aqueous dispersion and TEM imaging (Figure S1b) indicated that the FeO was well-dispersed on the GO nanosheets. After that, a uniform polypyrrole shell was coated on the GO nanosheets by oxidative polymerization. The rich oxygen-containing function groups on the GO nanosheets provide active sites for polypyrrole to grow uniformly on GO during polymerization.³⁰ The obtained product exhibited a sheet-like morphology and anchored FeO nanoparticles in Ppy (Figure S2), which finally underwent a carbonization treatment at $800 \text{ }^\circ\text{C}$ for 2 h under N_2 atmosphere to form the Fe-N-C/rGO catalyst.

SEM imaging of Fe-N-C/rGO (Figure 1a) revealed sheet-like structures, similar to that of the precursor before carbonization (Figure S2a and b), with no obvious aggregation which would favour a high specific surface area and exposure of active catalytic sites. TEM imaging

(Figure 1b-c) showed that Fe-N-C/rGO composite mainly contained sheet-like graphitic carbon and some small encapsulated nanoparticles. A corresponding HAADF-STEM image (Figure 1d) also revealed that small, high atomic number nanoparticles with an average size of 5 nm were embedded in mesoporous Fe-N-C/rGO.

XRD (Figure S3) of Fe-N-C/rGO showed a broad peak at around 25° confirming the existence of highly graphitized carbon; other diffraction peaks belonged to Fe_3O_4 (JCPDF No. 89-3854) and Fe_4C (JCPDF No. 89-4053). High-resolution TEM images (Figure S4a and b) revealed lattice spacings of 0.27 nm and 0.22 nm which match well with the (110) and (111) planes of Fe_4C . Figure S4c reveals lattice spacings of 0.29 nm and 0.24 nm coinciding with the (220) and (311) planes of Fe_3O_4 . As control samples, the N-C and N-C/rGO catalysts were also prepared. As shown in Figure S5a and b, the N-C catalysts carbonized from polypyrrole without rGO displayed an irregular structure with evident aggregation. However, when rGO was introduced into the system, the morphology of N-C/rGO changed into a non-aggregated sheet-like structure (Figure S6a and b). These results indicated that GO nanosheets served as the substrate structure providing nucleation sites for the uniform growth of polypyrrole, and avoiding aggregation of N-C/rGO during the carbonization process. Energy-dispersive X-ray (EDX) elemental maps in Figure 1d revealed that C, N, Fe are uniformly dispersed in the entire sheet-like Fe-N-C/rGO catalysts.

The elemental composition and surface electronic state of Fe-N-C/rGO catalyst was analyzed by XPS. The survey XPS spectrum (Figure S7a) indicated the presence of C (88.1 at.%), N (8.16 at.%), O (3.68 at.%) and Fe (0.15 at.%). As shown in Figure 2a, the high-resolution C 1s spectrum for Fe-N-C/rGO showed four peaks located at 284.65 eV,

285.20 eV, 286.15 eV, and 288.43 eV, which can be assigned to C-C, C-N, C-O and C=O groups, respectively.^{10,31} The corresponding high-resolution N 1s spectrum (Figure 2b) could be deconvoluted into four peaks at 398.2, 399.8, 400.9 and 402.5 eV, which are assigned to pyridinic-N, pyrrolic-N, graphitic-N and oxide-N, respectively.^{18,32,33} Moreover, the peak located at 398.2 eV may also belong to Fe-N_x coordination (~399.2 eV), because the difference between Fe-N_x coordination and pyridinic-N (398.2-399 eV) is too small to resolve within the uncertainty of the fit.³⁴ Pyridinic-N and graphitic-N in carbon have been reported to serve as efficient active sites for ORR.³⁵ Here, the amount of graphitic-N and pyridinic-N is 31.1% and 39.3% which would be expected to enhance the ORR performance. The high-resolution XPS spectrum of Fe 2p in Figure S7b reveals two pairs of peaks at 710.5 eV/722.7 eV and 714.2 eV/726.4 eV for Fe²⁺ and Fe³⁺, respectively,^{10,31,32} originating from the existence of Fe₃O₄ and Fe₄C in Fe-N-C/rGO.

The degree of graphitization of the catalysts was evaluated by Raman spectroscopy (Figure S8). Two peaks were observed around 1350 cm⁻¹ (D band) and 1580 cm⁻¹ (G band). Fe-N-C/rGO has a minimum ratio between the D and G band (I_D/I_G) intensities compared with the N-C and N-C/rGO. This demonstrates that the Fe-N-C/rGO catalysts have a high degree of graphitization. The specific surface areas and mesoporous features of Fe-N-C/rGO and reference catalysts were determined by N₂ adsorption-desorption isotherms. The results (Figure 2c, Figure S9, Table S1) indicated that Fe-N-C/rGO and N-C/rGO had a specific surface area of 477.81 m²/g and 436.36 m²/g, respectively, both of which were much higher than that of N-C (10.84 m²/g). This implies that rGO played a key role in reducing agglomeration and increasing the specific surface area of the catalysts. In addition, all of the

catalysts have an appropriate mesopore size distribution of around 3 nm. Therefore, Fe-N-C/rGO possessed the desired mesoporous structure with a high specific surface areas, favorable for mass transfer during the reaction process and the exposure of active sites.

The ORR performance of Fe-N-C/rGO and reference catalysts were precisely evaluated by detailed electrochemical tests. Firstly, the ORR activity of all catalysts was evaluated by cyclic voltammetry (CV) curves in N₂- and O₂-saturated 0.1 M KOH. As shown in the CV curves in Figure 3a, obvious cathodic reduction current peaks for all catalysts were observed in the O₂-saturated electrolyte, whilst no cathodic reduction current peak was found in the Ar-saturated electrolyte. The cathodic reduction current peak located at 0.74 V versus RHE of Fe-N-C/rGO was much higher than that of N-C/rGO (0.57 V) and N-C (0.56 V), implying that Fe-N-C/rGO had a better activity than Fe-C/rGO, N-C/rGO and N-C. Subsequently, Linear sweep voltammogram (LSV) curves (Figure 3b) were taken in the O₂-saturated electrolyte to investigate the ORR activity. The N-C catalysts exhibited the worst ORR activity with an onset potential of 0.80 V and a half-wave potential of 0.61 V, which is in agreement with the CV results. N-C/rGO catalysts displayed a similar onset potential of 0.80 V and a half-wave potential of 0.65 V. Importantly, when Fe was introduced into the system, Fe-N-C/rGO catalysts possessed the best ORR activity with an onset potential of 0.94 V and a half-wave potential of 0.81 V, which is comparable to the commercial Pt/C catalysts which showed an onset potential of 0.98 V and a half-wave potential of 0.82 V (Table S2).

To elucidate the ORR kinetic characteristics and catalytic pathway, the RDE system was used to derive LSV curves (Figure 3c), in which the limiting current density of Fe-N-C/rGO increased with the increasing electrode rotation rates. Corresponding Koutecky-Levich (K-L)

chinaXiv:201803.01552v1

plots (inset in Figure 3c) taken at different potentials showed nearly linear relationships, which implies first-order reaction kinetics with respect to the concentration of the dissolved oxygen in the solution.¹⁴ The transfer electron number (n) calculated from the K-L plots was in the range 3.8-4.0 from +0.3 V to +0.6 V, which indicated a direct $4e^-$ ORR process for the Fe-N-C/rGO catalyst. However, the transfer electron numbers of the N-C and N-C/rGO catalysts were estimated to be 2.7 and 2.3, respectively, from the K-L plots in Figure S10 which suggested a poor electron catalytic selectivity. In addition, as shown in Figure 3d, Fe-N-C/rGO catalysts revealed Tafel plot slopes of 98.8 mV dec^{-1} , which is comparable to that of Pt/C (93.7 mV dec^{-1}) and much lower than that of N-C ($157.3 \text{ mV dec}^{-1}$) and N-C/rGO ($160.9 \text{ mV dec}^{-1}$). These results imply Fe-N-C/rGO catalysts possessed a faster electron transfer rate than their counterparts.

The methanol crossover effect of Fe-N-C/rGO and Pt/C catalysts was evaluated from current versus time (I-t) plots following the injection of methanol into the electrolyte. Figure 4a showed no significant change in current for the Fe-N-C/rGO catalyst after the addition of methanol, unlike Pt/C catalysts which suffered a sharp increase due to the oxidation of methanol. This indicated that Fe-N-C/rGO had a better tolerance to methanol crossover than Pt/C. The stability of Fe-N-C/rGO and Pt/C catalysts was examined by chronoamperometric tests in O_2 -saturated 0.1 M KOH. As shown in Figure 4b, Fe-N-C/rGO catalysts displayed an excellent durability with a current loss of only 7.2% decay after 13000 s at a rotation rate of 1600 rpm. In comparison, Pt/C catalysts showed a rapid current loss with 20.8% decay under the same conditions.

As has been reported, the presence of Fe species is important in enhancing the ORR

activity of the Fe-N-C catalysts.^{9,10,36-38} Here we have shown that Fe-N-C/rGO catalysts contain Fe-based nanoparticles and also Fe-N_x active sites. However, it is unclear whether the Fe-based nanoparticles formed during the pyrolysis process are the reason for this enhanced activity.^{39,40} Therefore, we designed two control experiments: firstly, in order to estimate the contribution of Fe-based nanoparticles to the ORR activity, the Fe-N-C/rGO catalyst was leached in 0.5 M H₂SO₄ at 60 °C for 12 h to remove the Fe-based nanoparticles. TEM and HAADF-STEM images (Figure S11) revealed that most of the Fe-based nanoparticles disappeared after acid leaching. Related LSV curves (Figure 5a) indicated that the acid-leached Fe-N-C/rGO exhibited an 80 mV negative shift of the half-wave potential as compared with the original Fe-N-C/rGO material. This result demonstrated that the Fe-based nanoparticles act as active sites playing critical role in catalyzing ORR. Secondly, it is also known that the SCN⁻ ion can poison Fe-N_x active sites and suppress the ORR activity of the catalysts.^{41,42} Therefore, in a subsequent experiment, the ORR activity of Fe-N-C/rGO was measured in 0.5 M H₂SO₄ containing 0.01 M KSCN. The half-wave potential of Fe-N-C/rGO decreased significantly by 100 mV after the addition of 0.01 M KSCN, as shown in Figure 5b, which implies that the existence of Fe-N_x active sites is important to promote the ORR activity of Fe-N-C/rGO catalysts. Therefore, these two control experiments showed that both the Fe-based nanoparticles and Fe-N_x active sites are necessary to achieve the good ORR catalytic performance.

As described above, Fe-N-C/rGO catalysts possessed an ORR activity comparable to Pt/C with a much better durability and stronger tolerance against methanol crossover, which could be attributed to following reasons: (1) a high percentage of pyridinic-N (31.1%) and

graphitic-N (39.3%) doped into carbon can reduce the adsorption energy of O₂ because of the N doping-induced charge redistribution;^{17,43,44} (2) the presence of Fe impurities which form Fe-N_x coordinate sites and Fe-based nanoparticles embedded in carbon, both of which act as active sites during ORR;^{10,15,33,45} (3) the two-dimensional support material, rGO not only improves the exposure of active sites and the stability of catalysts, but also facilitates the charge transfer during the reaction process;^{26,27} (4) the mesoporous structure and high specific surface area of the catalysts is beneficial to the fast mass transport of reactants.

CONCLUSIONS

In summary, rGO-supported Fe-N-C(Fe-N-C/rGO) catalysts were fabricated by pyrolysis of a mixture of LAL-induced FeO nanoparticles, GO and PPy. Characterization reveals that the Fe-N-C/rGO catalyst consisted of Fe-N doped carbon with a few Fe-based nanoparticles (Fe₃O₄, Fe₄C), and exhibited a high specific surface area and mesoporous structure. Electrochemical tests indicated that Fe-N-C/rGO exhibited a superior ORR activity with an onset potential of 0.94 V and a half-wave potential of 0.81 V, which is comparable to Pt/C in alkaline media. The durability and tolerance against methanol crossover of Fe-N-C/rGO catalysts were much better than that of Pt/C catalysts. Control experiments confirmed that both Fe-based nanoparticles and Fe-N_x active sites can promote the ORR activity of the catalysts. The results of this work may provide a new route for fabrication of M-N/C electrocatalysts with a high-efficiency for metal-air batteries and fuel cells.

ASSOCIATED CONTENT

Supporting Information

SEM images, TEM images, XRD patterns, XPS spectra, Raman spectra, BET analysis and LSV analysis of Fe-N-C/rGO and the corresponding counterpart catalysts; table of specific surface area, pore volume, average pore size and ORR performance of Fe-N-C/rGO and the corresponding counterpart catalysts. This material is available free of charge via the Internet at <http://pubs.acs.org>.

AUTHOR INFORMATION

Corresponding Author

* Tel: +86 55165591129; Fax: Tel: +86 55165591434;

E-mail: chliang@issp.ac.cn

ACKNOWLEDGEMENTS

This work was financially supported by the National Basic Research Program of China (2014CB931704), the Instrument Developing Project of the Chinese Academy of Sciences (Grant No. YZ201627), the National Natural Science Foundation of China (NSFC, No.51371166, 11504375, 11404338, 11304315, 11674321, 51571186) and the Anhui Provincial Natural Science Foundation (1508085QA21). C. L also thanks the support from the Chinese Academy of Sciences/State Administration of Foreign Experts Affairs (CAS/SAFEA) International Partnership Program for Creative Research Teams.

REFERENCES

- (1) Winter, M.; Brodd, R. J. What Are Batteries, Fuel Cells, and Supercapacitors? *Chem. Rev.* **2005**, *105*, 4245–4269.
- (2) Armand, M.; Tarascon, J. M. Building better batteries. *Nature* **2008**, *451*, 652–657.
- (3) Debe, M. K. Electrocatalyst Approaches and Challenges for Automotive Fuel Cells. *Nature* **2012**, *486*, 43–51.
- (4) Guo, S.; Zhang, S.; Sun, S. Tuning Nanoparticle Catalysis for the Oxygen Reduction Reaction. *Angew. Chem. Int. Ed.* **2013**, *52*, 8526–8544.
- (5) Chen, C.; Kang, Y.; Huo, Z.; Zhu, Z.; Huang, W.; Xin, H. L.; Snyder, J. D.; Li, D.; Herron, J. A.; Mavrikakis, M.; Chi, M.; More, K. L.; Li, Y.; Markovic, N. M.; Somorjai, G. A.; Yang, P.; Stamenkovic, V. R. Highly Crystalline Multimetallic Nanoframes with Three-Dimensional Electrocatalytic Surfaces. *Science* **2014**, *343*, 1339–1343.
- (6) Xiao, M.; Zhu, J.; Feng, L.; Liu, C.; Xing, W. Meso/Macroporous Nitrogen-Doped Carbon Architectures with Iron Carbide Encapsulated in Graphitic Layers as an Efficient and Robust Catalyst for the Oxygen Reduction Reaction in Both Acidic and Alkaline Solutions. *Adv. Mater.* **2015**, *27*, 2521–2527.
- (7) Yin, P.; Yao, T.; Wu, Y.; Zheng, L.; Lin, Y.; Liu, W.; Ju, H.; Zhu, J.; Hong, X.; Deng, Z.; Zhou, G.; Wei, S.; Li, Y. Single Cobalt Atoms with Precise N-Coordination as Superior Oxygen Reduction Reaction Catalysts. *Angew. Chem. Int. Ed.* **2016**, *55*, 1–7.
- (8) Jaouen, F.; Proietti, E.; Lefevre, M.; Chenitz, R.; Dodelet, J. P.; Wu, G.; Chung, H. T.; Johnston, C. M.; Zelenay, P. Recent Advances in Non-precious Metal Catalysis for Oxygen-reduction Reaction in Polymer Electrolyte Fuel Cells. *Energy. Environ. Sci.* **2011**, *4*,

114–130.

(9) Liang, H. W.; Wei, W.; Wu, Z. S.; Feng, X.; Müllen, K. Mesoporous Metal–Nitrogen-Doped Carbon Electrocatalysts for Highly Efficient Oxygen Reduction Reaction. *J. Am. Chem. Soc.* **2013**, *135*, 16002–16005.

(10) Wu, Z.; Xu, X.; Hu, B.; Liang, H.; Lin, Y.; Chen, L.; Yu, S. H. Iron Carbide Nanoparticles Encapsulated in Mesoporous Fe-N-Doped Carbon Nanofibers for Efficient Electrocatalysis. *Angew. Chem. Int. Ed.* **2015**, *54*, 8179–8183.

(11) Wei, P.; Yu, G.; Naruta, Y.; Liu, J. G. Covalent Grafting of Carbon Nanotubes with a Biomimetic Heme Model Compound to Enhance Oxygen Reduction Reactions. *Angew. Chem. Int. Ed.* **2014**, *53*, 6659–6633.

(12) Wang, B.; Wang, X.; Zou, J.; Yan, Y.; Xie, S.; Hu, G.; Li, Y.; Dong, A. Simple-Cubic Carbon Frameworks with Atomically Dispersed Iron Dopants toward High-Efficiency Oxygen Reduction. *Nano Lett.* **2017**, *17*, 2003–2009.

(13) Yao, Y. F.; You, Y.; Zhang, G. X.; Liu, J. G.; Sun, H. R.; Zou, Z. G.; Sun, S. H. Highly Functional Bioinspired Fe/N/C Oxygen Reduction Reaction Catalysts: Structure-Regulating Oxygen Sorption. *ACS Appl. Mater. Interfaces* **2016**, *8*, 6464–6471.

(14) Liang, Y. Y.; Li, Y. G.; Wang, H. L.; Zhou, J. G.; Wang, J.; Regier, T.; Dai, H. J. Co₃O₄ Nanocrystals on Graphene as a Synergistic Catalyst for Oxygen Reduction Reaction. *Nat. Mater.* **2011**, *10*, 780–786.

(15) Wu, Z. S.; Yang, S. B.; Sun, Y.; Parvez, K.; Feng, X. L.; Müllen, K. 3D Nitrogen-Doped Graphene Aerogel-Supported Fe₃O₄ Nanoparticles as Efficient Electrocatalysts for the Oxygen Reduction Reaction. *J. Am. Chem. Soc.* **2012**, *134*,

9082–9085.

(16) Vigil, J. A.; Lambert, T. N.; Eldred, K. Electrodeposited MnO_x/PEDOT Composite Thin Films for the Oxygen Reduction Reaction. *ACS Appl. Mater. Interfaces* **2015**, *7*, 22745–22750.

(17) Gong, K. P.; Du, F.; Xia, Z. H.; Durstock M.; Dai L. M. Nitrogen-Doped Carbon Nanotube Arrays with High Electrocatalytic Activity for Oxygen Reduction. *Science* **2009**, *323*, 760–764.

(18) Men, B.; Sun, Y. Z.; Li, M. J.; Hu, C. Q.; Zhang, M.; Wang, L. A.; Tang, Y.; Chen, Y. M.; Wan, P. Y.; Pan, J. Q. Hierarchical Metal-Free Nitrogen-Doped Porous Graphene/Carbon Composites as an Efficient Oxygen Reduction Reaction Catalyst. *ACS Appl. Mater. Interfaces* **2016**, *8*, 1415–1423.

(19) Wu, G.; More, K. L.; Johnston, C. M.; Piotr, Z. High-Performance Electrocatalysts for Oxygen Reduction Derived from Polyaniline, Iron, and Cobalt. *Science* **2011**, *332*, 443–447.

(20) Fu, X. G.; Choi, J. Y.; Zamani, P.; Jiang, G. P.; Hoque, M. A.; Hassan, F. M.; Chen, Z. W. Co-N Decorated Hierarchically Porous Graphene Aerogel for Efficient Oxygen Reduction Reaction in Acid. *ACS Appl. Mater. Interfaces* **2016**, *8*, 6488–6495.

(21) Aijaz, A.; Masa, J.; Rçsler, C.; Xia, W.; Weide, P.; Botz, A. J. R.; Fischer, R. A.; Schuhmann, W.; Muhler, M. Co@Co₃O₄ Encapsulated in Carbon Nanotube-Grafted Nitrogen-Doped Carbon Polyhedra as an Advanced Bifunctional Oxygen Electrode. *Angew. Chem. Int. Ed.* **2016**, *55*, 4087–4091.

(22) Yin, P. Q.; Yao, T.; Wu, Y.; Zheng, L. R.; Lin, Y.; Liu, W.; Ju, H. X.; Zhu, J. F.;

Hong, X.; Deng, Z. X.; Zhou, G.; Wei, S. Q.; Li, Y. D. Single Cobalt Atoms with Precise N-Coordination as Superior Oxygen Reduction Reaction Catalysts. *Angew. Chem. Int. Ed.* **2016**, *55*, 1–7.

(23) Xia, W.; Zou, R. Q.; An, L.; Xia, D. G.; Guo, S. J. A Metal–organic Framework Route to in situ Encapsulation of Co@Co₃O₄@C Core@shell Nanoparticles into a Highly Ordered Porous Carbon Matrix for Oxygen Reduction. *Energy Environ. Sci.* **2015**, *8*, 568–576.

(24) Higgins, D.; Zamani, P. Y.; Yu, A. P.; Chen, Z. W. The Application of Graphene and Its Composites in Oxygen Reduction Electrocatalysis: a Perspective and Review of Recent Progress. *Energy Environ. Sci.* **2016**, *9*, 357–390.

(25) Sun, M.; Li, H. J.; Liu, Y.; Qu, J. H.; Li, J. H. Graphene-based Transition Metal Oxide Nanocomposites for the Oxygen Reduction Reaction. *Nanoscale* **2015**, *7*, 1250–1269.

(26) Li, J. S.; Wang, Y.; Liu, C. H.; Li, S. L.; Wang, Y. G.; Dong, L. Z.; Dai, Z. H.; Li, Y. F.; Lan, Y. Q. Coupled Molybdenum Carbide and Reduced Graphene Oxide Electrocatalysts for Efficient Hydrogen Evolution. *Nat. Commun.* **2016**, *7*, 11204–11212.

(27) Jiang, H. L.; Yao, Y. F.; Zhu, Y. H.; Liu, Y. Y.; Su, Y. H.; Yang, X. L.; Li, C. Z. Iron Carbide Nanoparticles Encapsulated in Mesoporous Fe-N-Doped Graphene-Like Carbon Hybrids as Efficient Bifunctional Oxygen Electrocatalysts. *ACS Appl. Mater. Interfaces* **2015**, *7*, 21511–21520.

(28) Hummers, W. S.; Offeman, R. E. Preparation of Graphitic Oxide. *J. Am. Chem. Soc.* **1958**, *80*, 1339.

(29) Xu, Y. X.; Bai, H.; Lu, G. W.; Li, C.; Shi, G. Q. Flexible Graphene Films via the

Filtration of Water-Soluble Noncovalent Functionalized Graphene Sheets. *J. Am. Chem. Soc.* **2008**, *130*, 5856–5857.

(30) Han, Y. Q.; Lu, Y. Preparation and Characterization of Graphite oxide/polypyrrole Composites. *Carbon* **2007**, *45*, 2394–2399.

(31) Zhang, Z. P.; Dou, M. L.; Liu, H. J.; Dai, L. M.; Wang F. A Facile Route to Bimetal and Nitrogen-Codoped 3D Porous Graphitic Carbon Networks for Efficient Oxygen Reduction. *Small* **2016**, *12*, 4193–4199.

(32) Niu, W. H.; Li, L. G.; Liu, X. J.; Wang, N.; Liu, J.; Zhou, W. J.; Tang, Z. H.; Chen, S. W. Mesoporous N- Doped Carbons Prepared with Thermally Removable Nanoparticle Templates: An Efficient Electrocatalyst for Oxygen Reduction Reaction. *J. Am. Chem. Soc.* **2015**, *137*, 5555–5562.

(33) Lin, L.; Zhu, Q.; Xu, A. W. Noble-Metal-Free Fe-N/C Catalyst for Highly Efficient Oxygen Reduction Reaction under Both Alkaline and Acidic Conditions. *J. Am. Chem. Soc.* **2014**, *136*, 11027–11033.

(34) Wu, G.; Johnston, C. M.; Mack, N. H.; Artyushkova, K.; Ferrandon, M.; Nelson, M.; Lezama-Pacheco, J. S.; Conradson, S. D.; More, K. L.; Myersd, D. J.; Zelenay, P. Synthesis–structure–performance Correlation for Polyaniline-Me-C Non-precious Metal Cathode Catalysts for Oxygen Reduction in Fuel Cells. *J. Mater. Chem.* **2011**, *21*, 11392–11405.

(35) Lai, L. F.; Potts, J. R.; Zhan, D.; Wang, L.; Poh, C. K.; Tang, C. H.; Gong, H.; Shen, Z. X.; Lin, J. Y.; Ruoff, R. S.; Exploration of the Active Center Structure of Nitrogen-doped Graphene-based Catalysts for Oxygen Reduction Reaction. *Energy Environ. Sci.* **2012**, *5*,

7936–7942.

(36) Ferrero, G. A.; Preuss, K.; Marinovic, A.; Jorge, A. B.; Mansor, N.; Brett, D. J. L.; Fuertes, A. B.; Sevilla, M.; Titirici, M. M.; Fe-N-Doped Carbon Capsules with Outstanding Electrochemical Performance and Stability for the Oxygen Reduction Reaction in Both Acid and Alkaline Conditions. *ACS Nano* **2016**, *10*, 5922–5932.

(37) Chen, P. Z.; Zhou, T. P.; Xing, L. L.; Xu, K.; Tong, Y.; Xie, H.; Zhang, L. D.; Yan, W. S.; Chu, W. S.; Wu, C. Z.; Xie, Y. Atomically Dispersed Iron-Nitrogen Species as Electrocatalysts for Bifunctional Oxygen Evolution and Reduction Reactions. *Angew. Chem. Int. Ed.* **2016**, *55*, 1–6.

(38) Qin, Y.; Yuan, J.; Zhang, L.; Zhao, B.; Liu, Y.; Kong, Y.; Cao, J. Y.; Chu, F. Q.; Tao, Y. X.; Liu, M. L. Rationally Designed 3D Fe and N Codoped Graphene with Superior Electrocatalytic Activity toward Oxygen Reduction. *Small* **2016**, *12*, 2549–2553.

(39) Strickland, K.; Miner, E.; Jia, Q. Y.; Tylus, U.; Ramaswamy, N.; Liang, W. T.; Sougrati, M. T.; Jaouen, F.; Mukerjee, S. Highly Active Oxygen Reduction Non-platinum Group Metal Electrocatalyst without Direct Metal-nitrogen Coordination. *Nat. Commun.* **2015**, *6*, 7343–7351.

(40) Kramm, U. I.; Geppert, I. H.; Behrends, J.; Lips, K.; Fiechter, S.; Bogdanoff, P.; On an Easy Way to Prepare Metal-Nitrogen Doped Carbon with Exclusive Presence of MeN_4^- type Sites Active for the ORR. *J. Am. Chem. Soc.* **2016**, *138*, 635–640.

(41) Wang, Q.; Zhou, Z. Y.; Lai, Y. J.; You, Y.; Liu, J. G.; Wu, X. L.; Terefe, E.; Chen, C.; Song, L.; Rauf, M.; Tian, N.; Sun, S. G. Phenylenediamine-Based FeN_x/C Catalyst with High Activity for Oxygen Reduction in Acid Medium and Its Active-Site Probing. *J. Am.*

Chem. Soc. **2014**, *136*, 10882–10885.

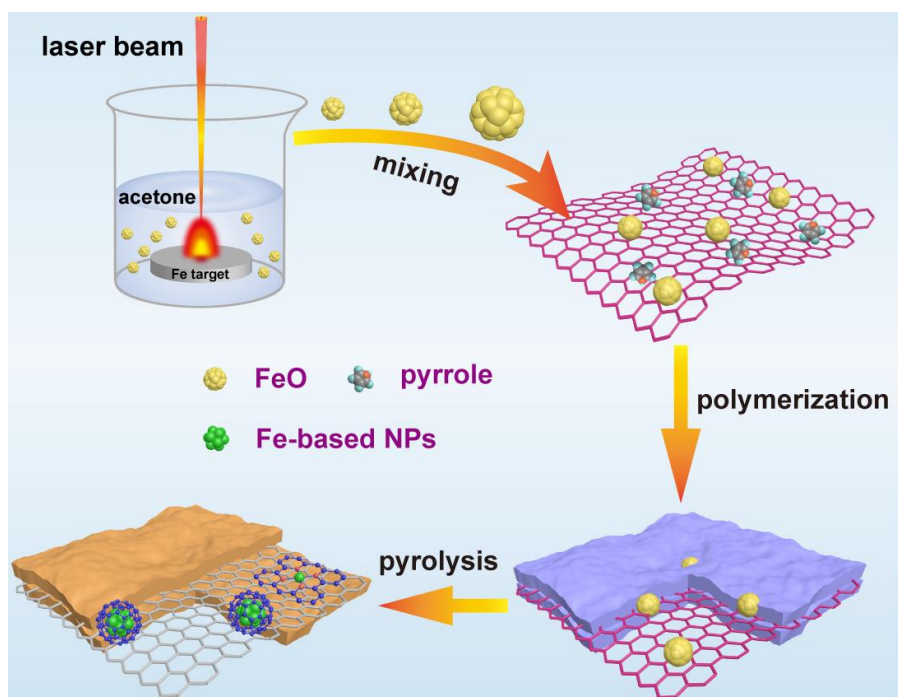
(42) Thorum, M. S.; Hankett, J. M.; Gewirth, A. A. Poisoning the Oxygen Reduction Reaction on Carbon-Supported Fe and Cu Electrocatalysts: Evidence for Metal-Centered Activity. *J. Phys. Chem. Lett.* **2011**, *2*, 295–298.

(43) Guo, D. H.; Shibuya, R.; Akiba, C.; Saji, S.; Kondo, T.; Nakamura, J. Active Sites of Nitrogen-doped Carbon Materials for Oxygen Reduction Reaction Clarified Using Model Catalysts. *Science* **2016**, *351*, 361–365.

(44) Liang, J.; Jiao, Y.; Jaroniec, M.; Qiao, S. Z. Sulfur and Nitrogen Dual-Doped Mesoporous Graphene Electrocatalyst for Oxygen Reduction with Synergistically Enhanced Performance. *Angew. Chem. Int. Ed.* **2012**, *51*, 11496–11500.

(45) Yang, W. X.; Liu, X. J.; Yue, X. Y.; Jia, J. B.; Guo, S. J. Bamboo-like Carbon Nanotube/Fe₃C Nanoparticle Hybrids and Their Highly Efficient Catalysis for Oxygen Reduction. *J. Am. Chem. Soc.* **2015**, *137*, 1436–1439.

Figures



Scheme 1. Schematic illustration of the fabrication process for Fe-N-C/rGO catalysts.

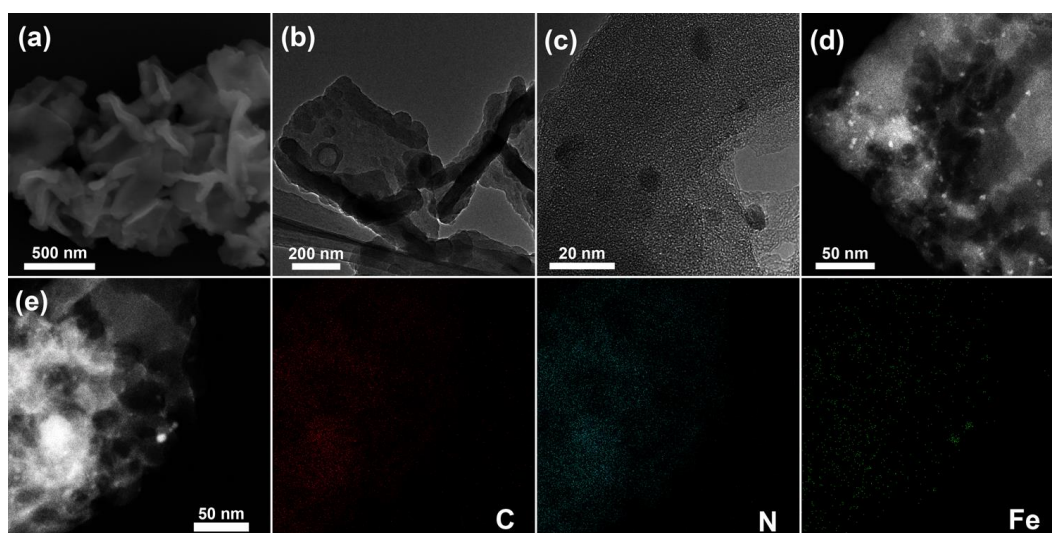


Figure 1. SEM image (a), TEM images (b-c) and HAADF-STEM image (d) of Fe-N-C/rGO. (e) shows a HAADF STEM image and corresponding EDX elemental maps of C, N, and Fe.

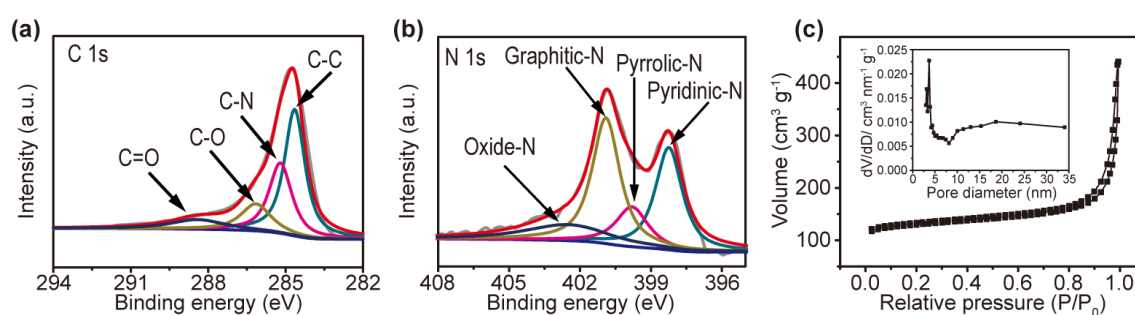


Figure 2. High-resolution C 1s XPS spectrum(a), N 1s XPS spectrum (b), (c) N_2 adsorption-desorption isotherm of Fe-N-C/rGO (inset: the corresponding pore size distribution).

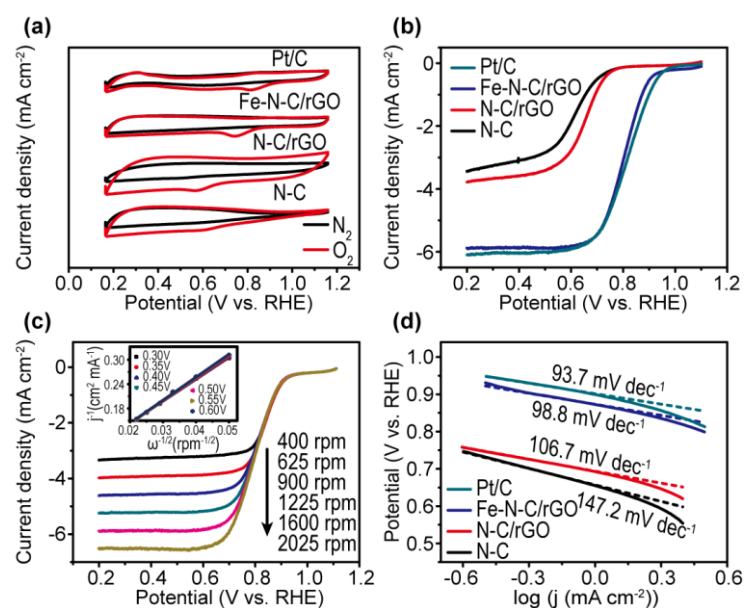


Figure 3. (a) Cyclic Voltammetry (CV) curves of Pt/C, Fe-N-C/rGO, N-C/rGO, N-C on glassy carbon electrodes in N₂- or O₂-saturated 0.1 M KOH solution at a scan rate of 50 mV s⁻¹, (b) Linear sweep voltammogram (LSV) curves of Pt/C, Fe-N-C/rGO, N-C/rGO, N-C in O₂-saturated 0.1 M KOH at a scan rate of 5 mV s⁻¹ with a rotation speed of 1600 rpm, (c) LSV curves of Fe-N-C/rGO in O₂-saturated 0.1 M KOH solution at a scan rate of 5 mV s⁻¹ with different rotation speeds (inset shows the corresponding K-L plots), (d) Tafel plots of Fe-N-C/rGO, N-C/rGO, N-C and commercial Pt/C catalysts.

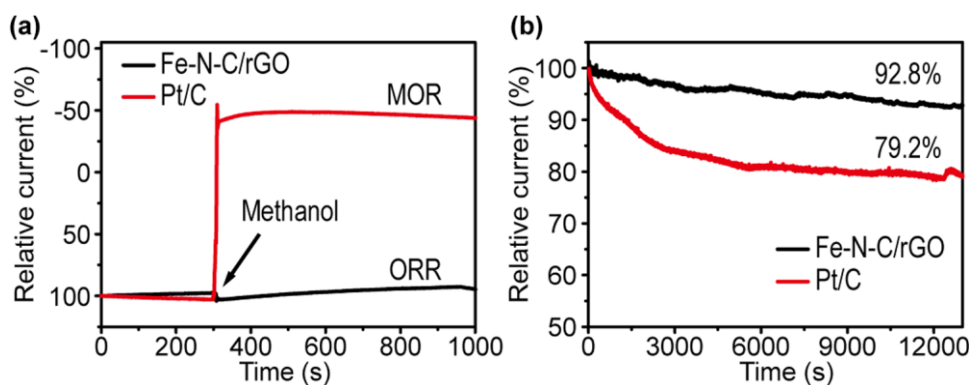


Figure 4. (a) Methanol-crossover from current versus time (I-t) chronoamperometric responses of the Fe-N-C/rGO and Pt/C in O₂-saturated 0.1 M KOH. The arrows indicate the addition of 5 mL methanol into the 80 mL solution after ≈ 300 s. (b) Durability tests of Fe-N-C/rGO and commercial Pt/C catalysts at an applied potential of 0.70 V versus RHE with a rotation speed of 1600 rpm in O₂-saturated 0.1 M KOH solution.

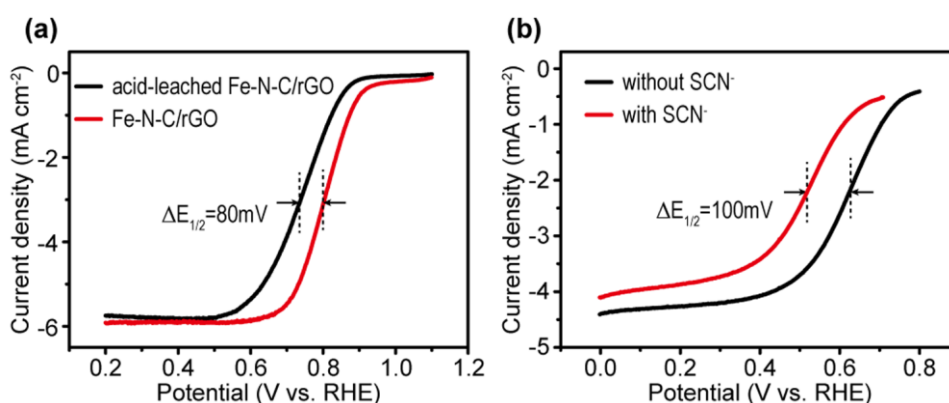


Figure 5. LSV curves of (a) acid-leached and as-prepared Fe-N-C/rGO catalysts in 0.1 M KOH, (b) Fe-N-C/rGO before and after the addition of 10 mM KSCN in 0.5 M H₂SO₄.

Table of Content (TOC) Graphic

